Materials
Horizons

COMMUNICATION

Cite this: *Mater. Horiz.*, 2022, **9**, 2450

Received 5th June 2022,
Accepted 19th July 2022

DOI: 10.1039/d2mh00698g

rsc.li/materials-horizons

Achieving circularly polarized luminescence and large piezoelectric response in hybrid rare-earth double perovskite by a chirality induction strategy†

Chang-Feng Wang, ‡[ab] Chao Shi, ‡[b] Anyi Zheng,‡[c] Yilei Wu,‡[d] Le Ye,[b]
Na Wang,[b] Heng-Yun Ye, [b] Ming-Gang Ju, *[d] Pengfei Duan, *[c]
Jinlan Wang *[d] and Yi Zhang *[abe]

Chirality, an intrinsic property of nature, has received increased attention in chemistry, biology, and materials science because it can induce optical rotation, ferroelectricity, nonlinear optical response, and other unique properties. Here, by introducing chirality into hybrid rare-earth double perovskites (HREDPs), we successfully designed and synthesized a pair of enantiomeric three-dimensional (3D) HREDPs, [(*R*)-*N*-methyl-3-hydroxylquinuclidinium]$_2$RbEu(NO$_3$)$_6$ (R1) and [(*S*)-*N*-methyl-3-hydroxylquinuclidinium]$_2$RbEu(NO$_3$)$_6$ (S1), which possess ferroelasticity, multiaxial ferroelectricity, high quantum yields (84.71% and 83.55%, respectively), and long fluorescence lifetimes (5.404 and 5.256 ms, respectively). Notably, the introduction of chirality induces the coupling of multiaxial ferroelectricity and ferroelasticity, which brings about a satisfactory large piezoelectric response (103 and 101 pC N^{-1} for R1 and S1, respectively). Moreover, in combination with the chirality and outstanding photoluminescence properties, circularly polarized luminescence (CPL) was first realized in HREDPs. This work sheds light on the design strategy of molecule-based materials with a large piezoelectric response and excellent CPL activity, and will inspire researchers to further explore the role of chirality in the construction of novel multifunctional materials.

New concepts

Materials possessing a large piezoelectric response and circularly polarized luminescence (CPL) have attracted wide attention due to their great application potential in lighting, displays, sensors, actuators, *etc.* However, the realization of CPL in three-dimensional (3D) hybrid perovskites and the precise design of hybrid perovskites with a large piezoelectric response have always been significant challenges but highly desired. Here, we demonstrate an effective design strategy for obtaining hybrid perovskites with a large piezoelectric response and 3D hybrid perovskites with excellent intrinsic CPL, that is, introducing chirality into hybrid rare-earth double perovskites (HREDPs). Following this design strategy, we successfully synthesized a pair of enantiomeric 3D HREDP luminescent ferroelectrics, [(*R*/*S*)-*N*-methyl-3-hydroxyl-quinuclidinium]$_2$RbEu(NO$_3$)$_6$, and therefore the intrinsic excellent CPL was realized in 3D HREDPs for the first time. Notably, the introduction of chirality achieves the coupling of multiaxial ferroelectricity and ferroelasticity, which brings about a large piezoelectric response, and reveals the unique role of chirality in the realization of large piezoelectric response. This work highlights that the chiral induction method and 3D HREDP system provide an efficient strategy and promising platform for the development of novel multifunctional materials.

1. Introduction

Chirality, one of the most important and basic attributes in nature, can couple with optics, electrics, magnetics, *etc.*, resulting in novel properties, such as circularly polarized luminescence (CPL), ferroelectricity and chiral magnetic effect.[1–3] Among them, CPL possessing numerous potential applications in optical information storage, three-dimensional (3D) displays, biological probes, *etc.*, has been one of hot topics in chiral materials research.[4–6] This is because chiral materials have the potential

---

[a] *Institute for Science and Applications of Molecular Ferroelectrics, Key Laboratory of the Ministry of Education for Advanced Catalysis Materials, Zhejiang Normal University, Jinhua, 321004, People's Republic of China*

[b] *Chaotic Matter Science Research Center, Faculty of Materials Metallurgy and Chemistry, Jiangxi University of Science and Technology, Ganzhou 341000, People's Republic of China*

[c] *CAS Center for Excellence in Nanoscience, CAS Key Laboratory of Nanosystem and Hierarchical Fabrication, National Center for Nanoscience and Technology (NCNST), No. 11, ZhongGuanCun BeiYiTiao, Beijing 100190, People's Republic of China. E-mail: duanpf@nanoctr.cn*

[d] *School of Physics, Southeast University, Nanjing 211189, People's Republic of China. E-mail: juming@seu.edu.cn, jlwang@seu.edu.cn*

[e] *Ordered Matter Science Research Center, Southeast University, Nanjing, 211189, People's Republic of China. E-mail: yizhang1980@seu.edu.cn*

† Electronic supplementary information (ESI) available: CCDC 2096217–2096223. For ESI and crystallographic data in CIF or other electronic format see DOI: **https://doi.org/10.1039/d2mh00698g**

‡ These authors contributed equally.

to directly emit different ratios of left and right CP light without using filters and polarizers.[3] Organic–inorganic hybrid halide perovskites (OIHHPs) have been demonstrated to possess high photoluminescence quantum yields, and they can get chiral properties by incorporating chiral organic cations.[2,7,8] Therefore, chiral OIHHPs have served as an intriguing and up-and-coming platform for developing CPL materials.[2,9,10] For instance, 1D chiral OIHHP (*R*/*S*)-3-(fluoropyrrolidinium)$MnBr_3$ with ferroelectricity and CPL activity were developed by Gao *et al.*[11] 2D chiral OIHHP (*R*/*S*-MBA)$_2PbI_4$ was found to possess a high average degree of CPL of 9.6% and 10.1%, respectively.[5] However, up to now, 3D chiral OIHHPs remain in a theoretically predicted stage, not to mention the 3D chiral OIHHPs with CPL activity, although they have wider applications, such as second-order nonlinear optical imaging and CP perovskite lasers.[2,12]

The main challenge in achieving intrinsic CPL activity in 3D OIHHPs is a structural constraint, *i.e.*, the Goldschmidt tolerance factor rule, which limits the 3D corner-shared framework only to accommodate relatively small-sized cations, such as MA^+, FA^+.[12,13] Fortunately, various pseudohalides, such as BF_4^-, NO_3^-, CH_3COO^-, *etc.*, have been explored and attempted to substitute halide anions to increase the cuboctahedral cage for accommodation of large chiral cation.[14] Rare-earth ions feature various coordination modes conducing to the construction of double perovskites and outstanding photoluminescent properties, such as narrow emission bands, high photoluminescence quantum yields and long luminescence lifetime.[15,16] Thus, hybrid rare-earth pseudohalide double perovskites are very suitable for the exploitation of 3D perovskite materials equipped with CPL.

On the other hand, chiral materials generally possess piezoelectricity naturally (except point group 432) due to the chiral structure being noncentrosymmetric, as exemplified by the first piezoelectric material, α-quartz adopting chiral point group 32. Piezoelectric materials that can convert mechanical energies into electrical energies, or *vice versa*, have attracted extensive attention, owing to their wide application in ultrasonic imaging, resonators, biological information sensors, and piezoelectric actuators.[17] Among them, inorganic ceramic ferroelectrics represented by lead zirconate titanate (PZT) have always occupied the mainstream of fundamental research and application, due to their large piezoelectric response and excellent environmental stability.[18–20] Recently, molecule-based piezoelectric materials have emerged as promising supplementary to traditional piezoelectric ceramics, owing to their lightweight, mechanically flexible, and solution-processing, but the piezoelectric performance of most of them is unsatisfactory, of which piezoelectric constant (d_{33}) less than 40 pC N^{-1}.[21,22] Notably, recent studies have shown that the coupling of multiaxial ferroelectricity and ferroelasticity is the key to obtaining large piezoelectric responses.[23,24] Nevertheless, how to accurately construct crystalline materials with the aforementioned features is still a thought-provoking problem.

Among 88 species of ferroelectric phase transition, there is a class of ferroelectrics (22 species) with a chiral-to-chiral phase transition feature, which provides a shortcut for the accurate design of multiaxial ferroelectrics coupled with ferroelasticity.[25] This is because 18 of the 22 species of chiral-to-chiral ferroelectric phase transitions have multiaxial nature. More importantly, among these 18 species of multiaxial ferroelectrics, 16 have ferroelasticity simultaneously (Table S1, ESI†). Therefore, introducing chirality into OIHPs might be a promising win-win design strategy for assembling materials with large piezoelectric response and CPL.

Herein, by molecular engineering strategies for decreasing symmetry and introducing chirality on quinuclidinium (Q) cations, we successfully obtained a pair of 3D chiral rare-earth double perovskite (HREDP) ferroelectrics, [(*R*)-*N*-methyl-3-hydroxylquinuclidinium]$_2$RbEu$(NO_3)_6$ (R1) and [(*S*)-*N*-methyl-3-hydroxylquinuclidinium]$_2$RbEu$(NO_3)_6$ (S1). R1 and S1 are multiaxial ferroelectric and ferroelastic simultaneously, and exhibit high quantum yields (84.71% and 83.55%, respectively) and long fluorescence lifetimes (5.404 and 5.256 ms, respectively). Notably, the synergy of chirality transfers from organic cations to inorganic frameworks and excellent photoluminescence properties of rare-earth ions endows 3D HREDPs with excellent intrinsic CPL for the first time. Moreover, entailing the virtue of order–disorder of orientations of organic cations and distortion of inorganic octahedra resulting from chirality transfer enable the coupling of multiaxial ferroelectricity with ferroelasticity in 3D HREDPs, leading to R1 and S1 with the exciting piezoelectric responses (103 pC N^{-1} and 101 pC N^{-1}, respectively). The combination of outstanding attributes of 3D HREDP systems and complementary advantages of chirality has provided an unprecedented insight into the design of novel multifunctional chiral materials.

2. Results and discussion

2.1. Design approach

Fig. 1A presents the summary process for the design strategy of chiral 3D HREDP ferroelectrics. Q cation with spherical configurations possesses minor rotational energy barriers.[26,27] Thus, we first adopted it as the template cations to construct the HREDPs, aiming to obtain ferroelectric phase transitions. However, due to the high symmetry for Q cation, the $(Q)_2RbEu(NO_3)_6$ adopts a centrosymmetric space group of $Fm\bar{3}m$ (point group, $m\bar{3}m$) at 293 K (Fig. 1B and Table S2, ESI†). Then, we sought to reduce the symmetry by adding a methyl group to the N atom of Q cation, yielding *N*-methyl-quinuclidinium cation, MeQ. The corresponding crystal structure transforms into a space group of $R\bar{3}$ (point group, $\bar{3}$). However, $(MeQ)_2RbEu(NO_3)_6$ is centrosymmetric, which is not allowed for ferroelectricity (Fig. 1C and Table S2, ESI†). The hydroxyl group was then added to MeQ, yielding *Rac*-*N*-methyl-3-hydroxylquinuclidinium cation, *Rac*-M3HQ, to further reduce the symmetry. Nevertheless, the obtained HREDP, [(*Rac*)-M3HQ]$_2$[RbEu$(NO_3)_6$] (*Rac*), is still non-polar (Fig. 1D and Table S2, ESI†). Therefore, we adopted the introduction of chirality, *i.e.*, using the homochiral organic cations, (*R*)-M3HQ and (*S*)-M3HQ, to construct the HREDPs. As expected, R1 and S1 crystallize in a chiral-polar space group of *R*3 (point group, 3) at 253 K (Table S3, ESI†). The enantiomorphic features for R1 and S1 were confirmed by circular dichroism (CD) spectra measurements (Fig. S1, ESI†).

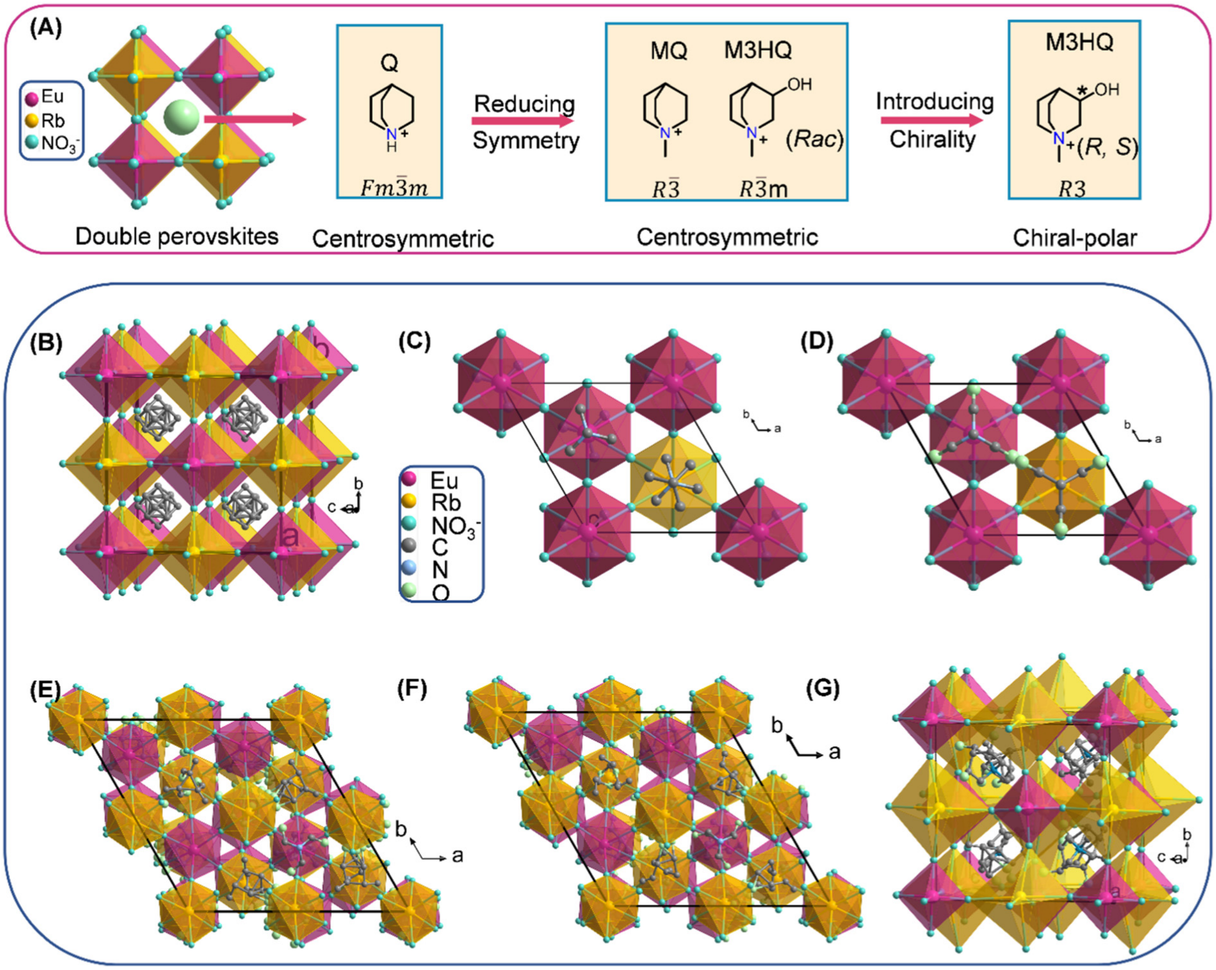

Fig. 1 Design strategy and crystal structures of 3D HREDPs. (A) Design strategy for R1 and S1. (B) $(Q)_2RbEu(NO_3)_6$ at 293 K. (C) $(MeQ)_2RbEu(NO_3)_6$ at 293 K. (D) *Rac* at 293 K. (E) S1 at 253 K. (F) R1 at 253 K. (G) R1 at 303 K. The NO_3^- ions are simplified as balls for clarity.

2.2. Reversible phase transition

The differential scanning calorimetry (DSC) results unambiguously disclose that R1 and S1 possess a reversible phase transition at about 285/279 K and 284/279 K in the heating/cooling run, respectively (Fig. S2, ESI†). Thus, the Curie temperatures (T_c) are determined as 285 and 284 K for R1 and S1, respectively. The small thermal hysteresis indicates that reversible phase transitions of R1 and S1 should belong to the second-order one. For the sake of simplicity, the phases above and below the T_c are labelled as high-temperature phase (HTP, corresponding to paraelectric phase) and low-temperature phase (LTP, corresponding to ferroelectric phase), respectively. From Fig. 1E and F, we can see that R1 and S1 adopt the elpasolite (K_2NaAlF_6) type of 3D double perovskite structure, where $Rb(NO_3)_6$ and $Eu(NO_3)_6$ octahedra adopting corner-sharing connectivity mode construct the 3D framework, and (*R*)-M3HQ and (*S*)-M3HQ organic cations were confined in the cages surrounded by the octahedra (Fig. S3, ESI†). In the LTP, the polar structure of R1 and S1 gives rise to a spontaneous polarization along the *c*-axis direction. In the HTP, the R1 and S1 adopt a chiral-non-polar space group of $P2_13$ (point group, 23), as shown in Fig. 1G. The number of symmetric elements changes from three (E, $2C_3$) to 12 (E, $8C_3$, $3C_2$), and thus R1 and S1 should belong to multiaxial ferroelectrics.[25] There are four equivalent spontaneous polarization along the four C_3 axes in the HTP (Fig. S4, ESI†). According to Aizu notation, R1 and S1 possess 23F3 type of multiaxial ferroelectric and ferroelastic phase transition simultaneously, which meets conditions for ferroelectrics with a large piezoelectric response proposed by pioneers.[23–25]

2.3. Ferroelasticity

Taking R1, for example, we demonstrate its ferroelastic, ferroelectric, and piezoelectric properties. Ferroelastic domains with different orientations possess different birefringence under perpendicular polarized light, which results in a contrast of light and dark patterns between them.[28] Therefore, we adopted polarized light microscopy with transmission mode to observe the evolution of the ferroelastic domains of R1 in the phase transition process. As shown in Fig. S5a (ESI†), the crystal of R1 displays uniform contrast in the HTP, agreeing well with that R1 belongs to the optically isotropic cubic system in the HTP.[29] When the crystal of R1 is in the LTP, the distinct striped ferroelastic domain pattern can be observed (Fig. 2A).

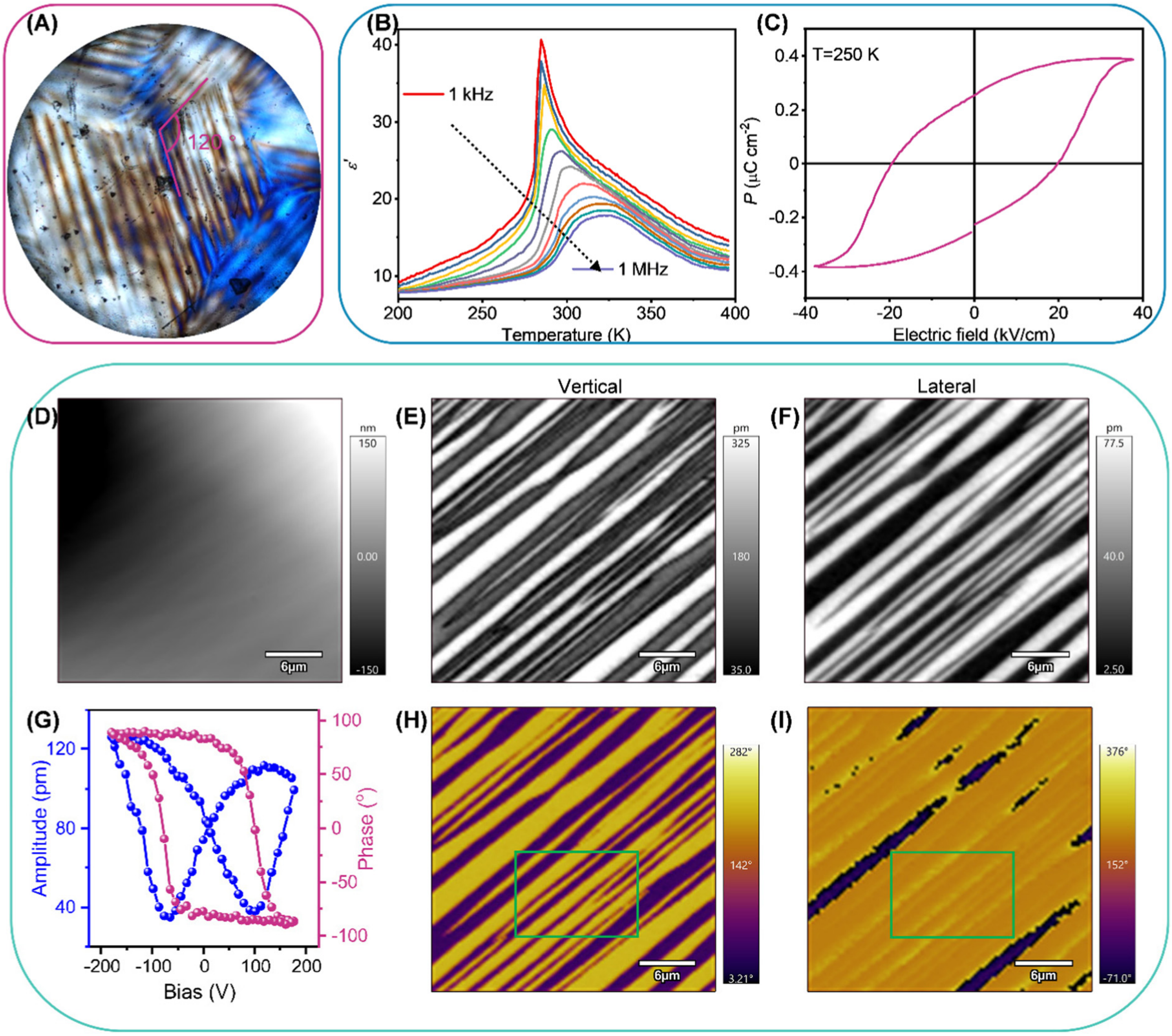

Fig. 2 Multiaxial ferroelastic and ferroelectric properties for R1. (A) Ferroelastic domains of R1 in the LTP. (B) The variable-temperature real part of dielectric constant (ε') measured on a single-crystal plate along the [111]-direction of HTP at different frequencies. (C) *P–E* loop measured on a single-crystal along the [111]-direction of HTP at 250 K. (D) Topography image. Vertical PFM amplitude (E) and phase (H) images. Lateral PFM amplitude (F) and phase (I) images. (G) Amplitude and phase as a function of bias voltage on a selected point.

The angles between intersecting domain patterns in R1 are close to 120°, which is should due to disappeared C_3 axes, confirming a multiaxial ferroelastic.[30] As crystal of R1 regressed from LTP to HTP, ferroelastic domains gradually diminished until they disappeared completely, indicating a reversible phase transition (Fig. S5b and c, ESI†).

2.4. Ferroelectricity

The reversible phase transitions, especially ferroelectric ones, commonly lead to anomalous dielectric responses at around phase transition temperature.[31,32] Thus, we performed the variable-temperature real part of complex dielectric constant (ε') measurements on a large-sized single-crystal of R1 along the [111]-direction of HTP at different frequencies to confirm the phase transition behavior. As shown in Fig. 2B, the curve of ε' *versus* temperature displays the λ-shape dielectric peaks at around T_c, indicating a second-order phase transition. Notably, the maximum value of the dielectric peak at different frequencies appears at different temperatures, which should result from the relaxation of phase transition behaviours.[33,34]

Due to the restriction of Kleinman symmetry, only 18 non-centrosymmetric point groups except three chiral point groups, 422, 432 and 622, have the second harmonic generation (SHG) signal response.[35,36] Therefore, we recorded the temperature-dependent SHG signal response to examine the symmetry breaking of the R1. As shown in Fig. S5d (ESI†), the SHG signal intensity at 210 K is 0.18 times as strong as that of KDP (KH_2PO_4), in line with R1 adopting a chiral-polar point group of 3 in the LTP. As the temperature increases to around the T_c, the SHG signal intensity exhibits a gradually decreasing trend, suggesting a second-order phase transition. Theoretically, R1 should possess SHG signal response in the HTP. However, when the temperature is above the T_c, the SHG signal intensity detected by the instrument is almost close to zero, which should because weak SHG signal intensity did not reach the lower detection limit of the instrument. Moreover, the SHG signal response intensity exhibits nice reversibility in the cooling run, demonstrating that the phase transition is reversible.

Ferroelectrics also possess pyroelectricity, which can transform the change of electric polarization induced by temperature to pyroelectric currents.[37] We implemented pyroelectric measurements on a large-sized single-crystal of R1 along [111]-direction of HTP in the heating mode. As depicted in Fig. S5e (ESI†), the pyroelectric current appears below T_c, corresponding to the chiral-polar point group of 3. As shown in Fig. S5f (ESI†), with the increase of temperature below T_c, the polarization values by integrating the pyroelectric current decrease gradually, according with the second-order phase transition feature.

To further confirm the ferroelectricity of R1, the double-wave method was employed to obtain the polarization-electric field (*P–E*) hysteresis loop. The obtained current density–electric field (*J–E*) curve presents two opposite peaks, ascribed to the polarization reversal caused by the electric field exceeding the coercive field (E_c) (Fig. S6, ESI†). As shown in Fig. 2C, the *P–E* loop calculated from the *J–E* loop displays well-shaped, which confirms the ferroelectricity of R1. The P_s (spontaneous polarization) and E_c of R1 are determined to be 0.38 μC cm^{-2} and 19.65 kV cm^{-1} at 250 K, respectively.

Piezoresponse force microscopy (PFM) has been amply proved to be a realizable tool that can non-destructively image and manipulate the domain structure of ferroelectrics at the nanoscale.[38] The vertical and the lateral PFM are utilized to detect the out-of- and in-plane polarization components, respectively. The amplitude and phase reflect the intensity of the piezoelectric response and direction of polarization, respectively. We employed the PFM to investigate the domain structure for R1 at 263 K. As shown in Fig. 2D, the domain patterns observed by the lateral and vertical PFM are not in agreement with topography, indicating that the response of signal results from the polarization state rather than topography. Taking the selected area as an example (green box), for the vertical PFM, the domain patterns observed from the amplitude and phase images display the stripe pattern with sharp contrast, revealing that out-of-plane polarization components of adjacent domains are in opposite directions (Fig. 2E and H), while, for the lateral PFM, the in-plane direction of polarization component of adjacent domains is the same (Fig. 2F and I). This result implies that the domains in this area are non-180°, suggesting that R1 belongs to multiaxial ferroelectrics.[39,40] To confirm R1 possessing switchable P_s, we performed the switching spectroscopy PFM (SS-PFM) on a selected point. The amplitude (blue line) and phase-bias loop (red line) are illustrated in Fig. 2G. The bias voltage exceeding the coercive voltage will give rise to phase reversal, indicating that R1 enjoys switchable P_s. The polarization switching with hysteresis behavior results in a butterfly-like amplitude-bias loop.

2.5. Origins for ferroelasticity and ferroelectricity in chiral HREDPs

In general, ferroelectrics are classified into two types, namely, order–disorder and displacive, which stems from polarization resulting from freezing and ordering of dipole moments that point in random directions in the HTP, and lattice instability resulting from long-range cooperative interaction produces a local polarization below the phase transition temperature, respectively. Traditional ferroelectricity is usually attributed to the displacive movement of a group of atoms. To understand the possible origins of ferroelectricity and ferroelasticity, the structure of *Rac*, R1 and S1 is investigated in detail. The intra-octahedral distortion of perovskites is further measured by the bond length distortion (Δd) and bond angle variance (σ^2) (Fig. S7a and b, ESI†). Here, Δd is defined as $\Delta d = (1/6)\Sigma(d_i - d_0)^2/d_0^2$, whereas σ^2 is defined as $\sigma^2 = \sum_{i=1}^{12}(\theta_i - 90)^2/11$.[41] Where d_i represents the M–N bond length (M = Rb, Eu), d_0 represents the average M–N bond length, and θ_i represents the N–M–N bond angles. Compared to *Rac*, R1 and S1 possess enhanced intra-octahedral distortions (Table S4, ESI†), which suggest that chiral molecules induce asymmetry of chiral perovskites (Fig. 3A). Notably, the perovskite framework of R1 and S1 still adopts a space group of *R*3, revealing that the chirality is successfully transferred from organic molecules to the perovskite framework (Fig. 3B). Therefore, the ferroelectricity of R1 and S1 might originate from both the orientation of organic molecules and

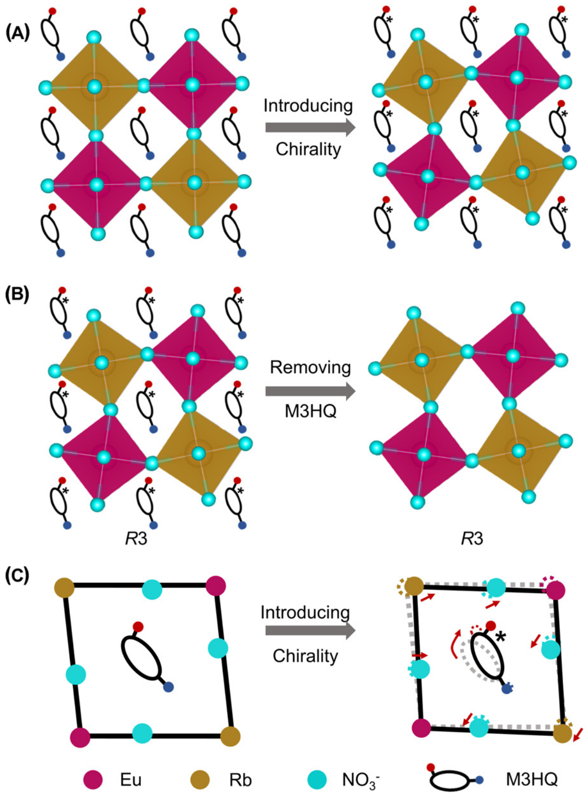

Fig. 3 Transfer of chirality in HREDPs. (A) The distortion originated from the introduction of chiral molecules. (B) The structure of R1 and R1 without M3HQ. (C) The displacive movements of atoms in octahedra originates from the rotation of M3HQ. The dashed circles represent atom positions before introducing chirality.

off-center displacement of metal cations in octahedra, in agreement with the previous study.[42]

Moreover, the rotation of aspherical organic cations in hybrid organic–inorganic perovskites can induce displacive movements of atoms in octahedra, leading to the ferroelasticity in perovskites.[43] The ferroelasticity of R1 and S1 could be attributed to the displacement of atoms derived from the rotation of M3HQ, which is a natural aspherical cation (Fig. 3C). In addition to chiral molecules, we speculated that the Coulomb repulsion between Eu $6s^2$ lone pair and nearby bonding electron pairs might lead to enhanced distortion of $Eu(NO_3)_6$ octahedra (Fig. S7C and Table S5, ESI†).[44] Further electronic structure analysis shows that the s orbital of Eu has a slight contribution to the charge density of HOMO−11, HOMO−12, and HOMO−13 (Fig. S8 and S9, ESI†). Through above analysis, it is significant that the transfer of chirality from organic cations to inorganic framework trigger coupling of multiaxial ferroelectricity and ferroelasticity in chiral perovskites, which provide effective strategy to rational design of materials with large piezoelectric responses.

2.6. Piezoelectricity

Using the PFM technique, we first performed the local piezoelectric response measurements to evaluate the piezoelectric properties of R1. The results of measurements were compared with those of widely used piezoelectric materials, PVDF and $LiNbO_3$. A conductive probe tip with a bias voltage of 1 V was adopted to drive each film across the resonant frequency. The piezoelectric response curves are shown in Fig. 4A. The clear resonance peaks for R1, PVDF, and $LiNbO_3$ are observed at 352, 311, and 366 kHz, respectively. The effective amplitudes were obtained by dividing amplificatory amplitude by quality factor (Q factor).[38] As shown in Fig. 4A, the resonance peak in R1 film is the highest, indicating that R1 possesses a stronger intensity of piezoelectric response than PVDF and $LiNbO_3$. The amplitude plots as a function of bias voltage present good linear relation, confirming that the response results from inherent piezoelectricity (Fig. 4B). The quasi-static (Berlincourt) method was employed to determine the reliable and accurate piezoelectric properties (Fig. 4C and Fig. S10, ESI†).[23] In measurement, the normal stress was applied on a large-sized and high-quality single crystal of R1 along the [111]-direction of HTP. As shown in Fig. 4C, the single crystal of R1 possesses a large piezoelectric coefficient (d_{33}) up to about 103 pC N^{-1}, superior to that of the most recently reported molecule-based and quite a few conventional piezoelectric materials (Fig. 4D).[23,45,46] We also measured the piezoelectric properties for S1, the obtained d_{33} is about 101 pC N^{-1} (Fig. S10, ESI†).

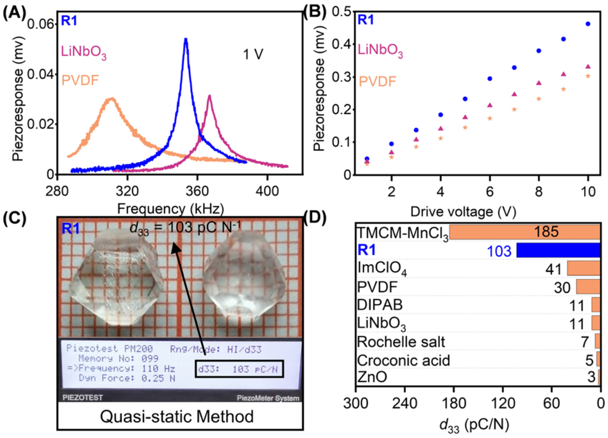

Fig. 4 Piezoelectric properties of R1. (A) PFM response peaks of PVDF, R1, and $LiNbO_3$. (B) PFM amplitude signal of PVDF, R1, and $LiNbO_3$ at different drive voltages. (C) Piezoelectric constant (d_{33}) measurement of R1, using quasi-static (Berlincourt) method. (D) Piezoelectric coefficient of R1 compared with that of other piezoelectrics. Including TMCM–$MnCl_3$ (trimethylchloromethyl ammonium trichloromanganese), $ImClO_4$ (imidazolium perchlorate), PVDF, DIPAP (diisopropylammonium bromide), $LiNbO_3$, Rochelle salt, croconic acid and ZnO.

Compared to the uniaxial ferroelectrics, whose polarization only can be reversed, multiaxial ferroelectrics can have multiple alternative directions. Therefore, when the external stress is applied, the polarization will select a direction with the minimum energy barrier to switch. Meanwhile, R1 having 23F3 type of phase transition belongs to fully ferroelectric/fully ferroelastic, indicating its ferroelectric and ferroelastic domains to be identical.[23] When external stress gives rise to the switch of strain state, the polarization state is also switched. Such switch of low energy barriers, and coupling effect of ferroelectricity and ferroelasticity significantly promotes the polarization change, which results in a satisfactory piezoelectric response.

2.7. Photoluminescence and CPL properties

One of the advantages of HREDPs is possessing excellent photoluminescence properties. As shown in inset of Fig. S11a (ESI†), the colorless crystal of R1 emits red photoluminescence under UV light (365 nm). The excitation and emission spectra for R1 are presented in Fig. S11a (ESI†). There are two strong emissions at 592 and 616 nm, respectively. The 592 and 616 nm emissions are derived from ${}^5D_0 \rightarrow {}^7F_1$ magnetic dipole transition, and ${}^5D_0 \rightarrow {}^7F_2$ electric dipole transition, respectively. S1 possesses similar photoluminescence properties (Fig. S12, ESI†).[47] R1 and S1 possess superior photoluminescence properties. For one thing, R1 and S1 exhibit relatively high quantum yields, 84.71%, 83.5%, respectively (Fig. S11b and S13, ESI†). For another, the fluorescence lifetime of R1 and S1 is 5–30 times that of reported Mn-based molecular luminescent ferroelectric materials (Fig. S11c and S13, ESI†).[23,48–51]

Motivated by the excellent photoluminescence and homochiral characteristics, we further explored chiroptical properties in the excited state of R1 and S1 by testing the CPL spectra. As illustrated in Fig. 5A and B, crystals of R1 and S1 show mirror-image CPL signals from 580–630 nm excited by 397 nm light from a Xe lamp. The emission peaks located at 588 nm and 613 nm are attributed to Eu^{3+} ${}^5D_0 \rightarrow {}^7F_1$ and ${}^5D_0 \rightarrow {}^7F_2$ transitions, respectively, which is consistent with the photoluminescence spectra. To verify the authenticity of the CPL signals, we have measured the CPL spectra by rotating the crystals at different angles (90°, 180°, 270°) perpendicular to the testing direction (Fig. S14, ESI†). The obtained CPL signals are

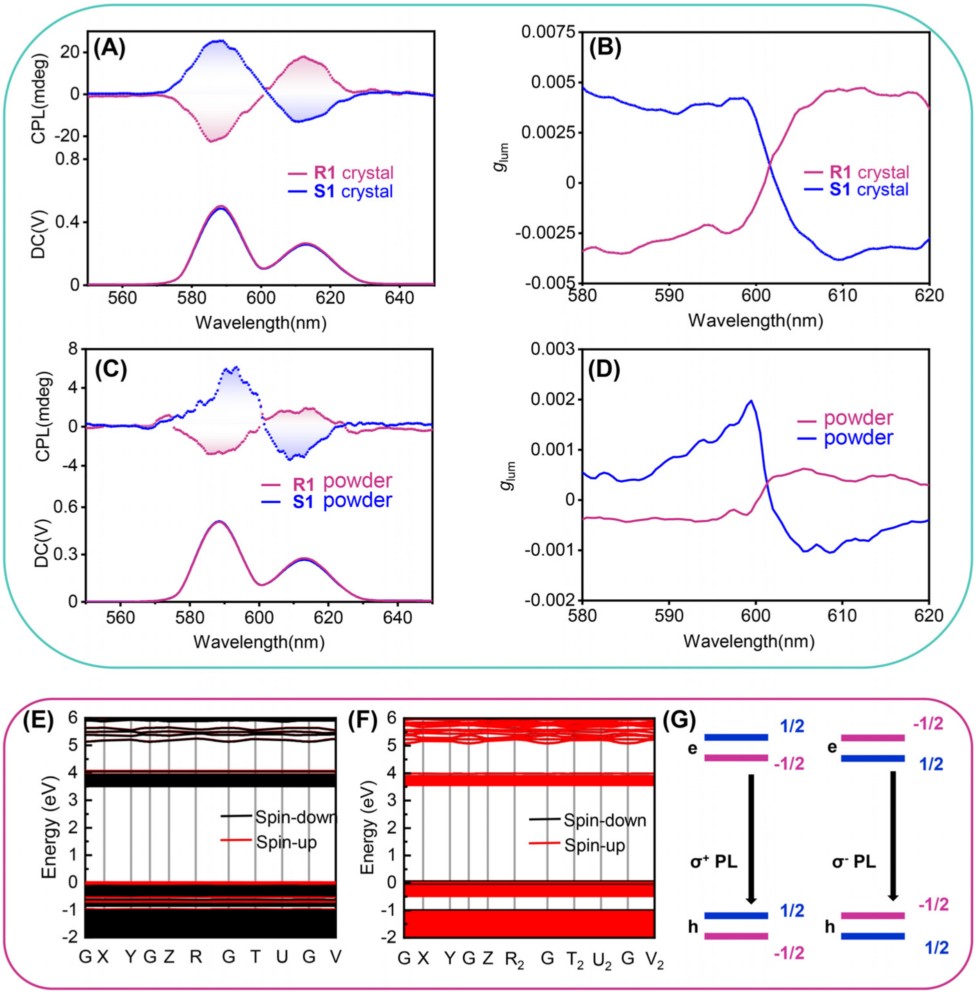

Fig. 5 CPL properties measured at room temperature and DFT results of CPL in HREDPS. (A) CPL spectra of S1 (blue line) and R1 (red line) crystal samples excited by 397 nm. (B) The g_{lum} *vs.* wavelength curves of crystal samples. (C) CPL spectra of S1 (blue line) and R1 (red line) powder samples excited by 397 nm. (D) The g_{lum} *vs.* wavelength curves of powder samples. The DFT-calculated band structure of (E) R1 and (F) S1. (G) The mechanism of CPL.

almost the same in different testing angles without obvious change. These results indicate that the CPL signal is independent of the testing angle of the crystals. Thus, the obtained CPL signals of the crystals were plausible.

Besides, R1 and S1 powder could also be used to confirm the chiroptical properties in an excited state. We have measured the CPL spectra of the corresponding powders made by grinding the crystals. Clearly, the powders also showed identical mirror-image CPL signals (Fig. 5C and D), although the intensity seems a little weaker than the crystals. Luminescence dissymmetry factor (g_{lum}) can be used to evaluate the level of CPL property, $g_{lum} = 2 \times (I_L - I_R)/(I_L + I_R)$, where I_L and I_R are the intensity of the left- and right-hand CPL, respectively.[52] The g_{lum} factors of R1 and S1 crystals are calculated as -2.9×10^{-3} and 3.6×10^{-3} at 588 nm, 4.4×10^{-3} and -3.3×10^{-3} at 613 nm, respectively (Table S6, ESI†). In comparison, the g_{lum} factors of R1 and S1 powder are -3.9×10^{-4} and 5.9×10^{-4} at 588 nm, 4.9×10^{-4} and -7.7×10^{-4} at 613 nm, respectively, which are smaller than crystalline state. This might be due to the strong scattering in powder samples, as well as the less ordering stacking.

To investigate the origin of chiroptical properties of R1 and S1, we performed spin-polarized density functional theory (DFT) calculations (Fig. 5E and F). R1 and S1 possess a wide bandgap of 3.37 and 3.50 eV, respectively. It is noted that the conduction band and the valence band near the Fermi level are both flat bands, suggesting the localization of electrons and holes. More importantly, electronic structures in spin-down and spin-up channels are separate, leading to the opposite spin polarization between the valence band maximum (VBM) and the conduction band minimum (CBM). Previous studies revealed that the different rates of spin-polarized emission resulted in the selected polarized photoluminescence, corresponding to the CPL (Fig. 5G).[53] In this case of R1, the spin flipping from spin-up to spin-down is energetically favorable, leading to the emission of the right (σ^+) CPL. As for S1, the photophysical process is similar. From a material design perspective, a vital question is what role chiral molecules play in the CPL of chiral perovskites. We replaced chiral organic cations with a background charge density and calculated the electronic structure of the octahedral corner-sharing framework of R1 and S1 (Fig. S15, ESI†). The opposite spin polarization between VBM and CBM suggested that the CPL originates from the perovskite framework. Moreover, for small molecules, the emission of circularly polarized light is proportional to the g factor, which is defined as $g = \frac{4|\mu||m|\cos\theta}{|\mu|^2+|m|^2}$. Where μ and m are the transition electric dipole moment and transition magnetic dipole moment, respectively.[54] Table S7 (ESI†) shows that the CPL of R1 and S1 is mainly contributed by $Eu(NO_3)_6^{3-}$, suggesting the successful chirality transfer from organic cations to perovskite framework.

To date, endowing 3D perovskites with CPL activity remains a big challenge. Several strategies have been proposed, including co-assembly with chiral matrix in nonpolar solvents, surface-lattice distortion of chiral amine, capping chiral ammonium on the surface of perovskite nanocrystals by ligand treatment.[55–57] Lattices of these kinds of perovskites are achiral, that is, they don't have intrinsic chirality. Here, we have successfully constructed intrinsic chiral bulky crystals with bright photoluminescence and CPL properties. A-site chiral organic cations could induce perovskites to form chiral-polar space groups, and the luminescent Eu^{3+} ions are in an intrinsic chiral environment, enabling R1 and S1 with excellent CPL activity.

3. Conclusions

In summary, we have successfully achieved a pair of chiral 3D HREDP ferroelectrics, R1 and S1, possessing large piezoelectric response (103 and 101 pC N^{-1}, respectively), and CPL activity, by introducing chirality and selecting photoluminescent $RbEu(NO_3)_6$ scaffold to assemble crystal lattice. Variable-temperature single-crystal X-ray diffraction disclosed that R1 and S1 belong to the 23F3 type of full ferroelectric/full ferroelastic phase transition. Utilizing polarized light microscopy, the evolution of the ferroelastic domain in the phase transition process was observed. Vectorial PFM well demonstrated multiaxial ferroelectricity. The coupling of multiaxial ferroelectricity and ferroelasticity endows R1 and S1 an impressive piezoelectric response. In addition, chirality induced the CPL activity of the R1 and S1 with excellent photoluminescence properties. This work illustrates the important role that chirality plays in the piezoelectricity and CPL properties of ferroelectrics, and will encourage more researchers to investigate the effect of chirality on other related properties.

4. Experimental section

4.1. Synthesis

Quinuclidinium (Q) nitrates (4 mmol, 0.7 g), $Eu(NO_3)_3\ 6H_2O$ (2 mmol, 0.892 g), and $RbNO_3$ (2 mmol, 0.295 g) were dissolved in a water solution (20 mL). The solution was stirred at room temperature until completely dissolved, and then evaporated at room temperature. After 2–3 days, the colorless bulk single-crystal of $(Q)_2RbEu(NO_3)_6$ precipitated at the bottom of the beaker. The synthesis method and large-sized crystal preparation of $(MeQ)_2RbEu(NO_3)_6$, $[(Rac)\text{-M3HQ}]_2[RbEu(NO_3)_6]$, R1, and S1 were the same as that for $(Q)_2RbEu(NO_3)_6$.

4.2. Experimental characterization

Detail information on crystal structure determination, CD spectrum measurement, CPL measurements, polarized light microscopy measurements, SHG measurements, variable-temperature dielectric permittivity measurements, pyroelectric property measurements, *P–E* hysteresis loops measurements, piezoresponse force microscopy measurements, piezoelectric measurements, photoluminescence measurements and DFT calculations is included in ESI.†

4.3. Computational methods

The first-principles calculations for R1 and S1 were performed based on density functional theory implemented in the Vienna ab initio Simulation Package.[58] The projector-augmented wave method with the generalized gradient approximation of the Perdew–Burke–Ernzerhof exchange–correlation functional was used.[59,60] The transition electric dipole moment and transition magnetic dipole moment of MA, R-M3HQ$^+$, S-M3HQ$^+$, and $Eu(NO_3H)_6^{3+}$ were calculated in the framework of time-dependent density functional theory by using the Gaussian code.[61] The orbitals of $Eu(NO_3H)_6^{3+}$ are plotted by utilizing the Multiwfn software.[62]

4.4. Single crystal structure information

CCDC 2096217–2096223 contains the supplementary crystallographic data for this paper.†

Author contributions

Prepare samples: Le Ye; ferroelectric properties related measurements: Chao Shi; PFM measurements: Na Wang; CPL measurements: Anyi Zheng; DFT calculations: Yilei Wu; Research suggestions: Heng-Yun Ye; writing – original draft: Chang-Feng Wang and Ming-Gang Ju; writing – review & editing: Jinlan Wang, Pengfei Duan, and Yi Zhang.

Conflicts of interest

There are no conflicts to declare.

Acknowledgements

This work was supported by National Key Research and Development Program of China (Grant No. 2017YFA0204800); National Natural Science Foundation of China (92056112; 91856115; 22173019); Strategic Priority Research Program of Chinese Academy of Sciences (No. XDB36000000).

Notes and references

1 H. N. Yu, C. Welch, W. T. Qu, C. J. Schubert, F. Liu, G. Siligardi and G. H. Mehl, *Mater. Horiz.*, 2020, 7, 3021–3027.

2 G. Long, R. Sabatini, M. I. Saidaminov, G. Lakhwani, A. Rasmita, X. Liu, E. H. Sargent and W. Gao, *Nat. Rev. Mater.*, 2020, **5**, 423–439.

3 J. R. Brandt, F. Salerno and M. J. Fuchter, *Nat. Rev. Chem.*, 2017, **1**, 0045.

4 R. Pan, K. Wang and Z.-G. Yu, *Mater. Horiz.*, 2022, **9**, 740–747.

5 J. Ma, C. Fang, C. Chen, L. Jin, J. Wang, S. Wang, J. Tang and D. Li, *ACS Nano*, 2019, **13**, 3659–3665.

6 C. Dee, F. Zinna, E. Kreidt, L. Arrico, A. Rodríguez-Rodríguez, C. Platas-Iglesias, L. Di Bari and M. Seitz, *J. Rare Earths*, 2020, **38**, 564–570.

7 K. P. Goetz, A. D. Taylor, F. Paulus and Y. Vaynzof, *Adv. Funct. Mater.*, 2020, **30**, 1910004.

8 F. Wang, H. Gao, C. de Graaf, J. M. Poblet, B. J. Campbell and A. Stroppa, *npj Comput. Mater.*, 2020, **6**, 183.

9 J. T. Lin, D. G. Chen, L. S. Yang, T. C. Lin, Y. H. Liu, Y. C. Chao, P. T. Chou and C. W. Chiu, *Angew. Chem., Int. Ed.*, 2021, **60**, 21434–21440.

10 J. Ahn, E. Lee, J. Tan, W. Yang, B. Kim and J. Moon, *Mater. Horiz.*, 2017, **4**, 851–856.

11 J. X. Gao, W. Y. Zhang, Z. G. Wu, Y. X. Zheng and D. W. Fu, *J. Am. Chem. Soc.*, 2020, **142**, 4756–4761.

12 G. Long, Y. Zhou, M. Zhang, R. Sabatini, A. Rasmita, L. Huang, G. Lakhwani and W. Gao, *Adv. Mater.*, 2019, **31**, 1807628.

13 C. Katan, N. Mercier and J. Even, *Chem. Rev.*, 2019, **119**, 3140–3192.

14 J. Chen and N.-G. Park, *Small Methods*, 2021, **5**, 2100311.

15 F. Zinna and L. Di Bari, *Chirality*, 2015, **27**, 1–13.

16 J. Ma, Q. Xu, L. Ye, Q. Wang, Z. Gong, C. Shi, H. Ye and Y. Zhang, *J. Rare Earths*, 2022, **40**, 937–941.

17 G. Rui, E. Allahyarov, R. Li, P. L. Taylor and L. Zhu, *Mater. Horiz.*, 2022, **9**, 1992–1998.

18 L. You, F. Zheng, L. Fang, Y. Zhou, L. Z. Tan, Z. Zhang, G. Ma, D. Schmidt, A. Rusydi, L. Wang, L. Chang, A. M. Rappe and J. Wang, *Sci. Adv.*, 2018, **4**, eaat3438.

19 Z. Chen, Z. Li, M. Ma, T. Zhao, J. Qiu and J. Ding, *J. Rare Earths*, 2018, **36**, 745–749.

20 J. Dai, P. Du, J. Xu, C. Xu and L. Luo, *J. Rare Earths*, 2015, **33**, 391–396.

21 C. R. Huang, Y. Li, Y. Xie, Y. Du, H. Peng, Y. L. Zeng, J. C. Liu and R. G. Xiong, *Angew. Chem., Int. Ed.*, 2021, **60**, 16668–16673.

22 Z. X. Wang, H. Zhang, F. Wang, H. Cheng, W. H. He, Y. H. Liu, X. Q. Huang and P. F. Li, *J. Am. Chem. Soc.*, 2020, **142**, 12857–12864.

23 Y. M. You, W. Q. Liao, D. Zhao, H. Y. Ye, Y. Zhang, Q. Zhou, X. Niu, J. Wang, P. F. Li, D. W. Fu, Z. Wang, S. Gao, K. Yang, J. M. Liu, J. Li, Y. Yan and R. G. Xiong, *Science*, 2017, **357**, 306–309.

24 Y. Hu, L. You, B. Xu, T. Li, S. A. Morris, Y. Li, Y. Zhang, X. Wang, P. S. Lee, H. J. Fan and J. Wang, *Nat. Mater.*, 2021, **20**, 612–617.

25 K. Aizu, *J. Phys. Soc. Jpn.*, 1969, **27**, 387–396.

26 W.-Y. Zhang, Y.-Y. Tang, P.-F. Li, P.-P. Shi, W.-Q. Liao, D.-W. Fu, H.-Y. Ye, Y. Zhang and R.-G. Xiong, *J. Am. Chem. Soc.*, 2017, **139**, 10897–10902.

27 J. Harada, Y. Kawamura, Y. Takahashi, Y. Uemura, T. Hasegawa, H. Taniguchi and K. Maruyama, *J. Am. Chem. Soc.*, 2019, **141**, 9349–9357.

28 E. Strelcov, Q. Dong, T. Li, J. Chae, Y. Shao, Y. Deng, A. Gruverman, J. Huang and A. Centrone, *Sci. Adv.*, 2017, **3**, e1602165.

29 H. Y. Zhang, C. L. Hu, Z. B. Hu, J. G. Mao, Y. Song and R. G. Xiong, *J. Am. Chem. Soc.*, 2020, **142**, 3240–3245.

30 Z. B. Liu, L. He, P. P. Shi, Q. Ye and D. W. Fu, *J. Phys. Chem. Lett.*, 2020, **11**, 7960–7965.

31 C. Shi, J. J. Ma, J. Y. Jiang, M. M. Hua, Q. Xu, H. Yu, Y. Zhang and H. Y. Ye, *J. Am. Chem. Soc.*, 2020, **142**, 9634–9641.

32 A. García-Fernández, J. M. Bermúdez-García, S. Castro-García, A. L. Llamas-Saiz, R. Artiaga, J. López-Beceiro, S. Hu, W. Ren, A. Stroppa, M. Sánchez-Andújar and M. A. Señarís-Rodríguez, *Inorg. Chem.*, 2017, **56**, 4918–4927.

33 H. Y. Ye, W. Q. Liao, Q. Zhou, Y. Zhang, J. Wang, Y. M. You, J. Y. Wang, Z. N. Chen, P. F. Li, D. W. Fu, S. D. Huang and R. G. Xiong, *Nat. Commun.*, 2017, **8**, 14551.

34 L. E. Cross, *Ferroelectrics*, 1987, **76**, 241–267.

35 D. A. Kleinman, *Phys. Rev.*, 1962, **126**, 1977–1979.

36 K. Li, Z. G. Li, J. Xu, Y. Qin, W. Li, A. Stroppa, K. T. Butler, C. J. Howard, M. T. Dove, A. K. Cheetham and X. H. Bu, *J. Am. Chem. Soc.*, 2022, **144**, 816–823.

37 C. F. Wang, H. Li, M. G. Li, Y. Cui, X. Song, Q. W. Wang, J. Y. Jiang, M. M. Hua, Q. Xu, K. Zhao, H. Y. Ye and Y. Zhang, *Adv. Funct. Mater.*, 2021, **31**, 2009457.

38 H. Y. Zhang, X. G. Chen, Y. Y. Tang, W. Q. Liao, F. F. Di, X. Mu, H. Peng and R. G. Xiong, *Chem. Soc. Rev.*, 2021, **50**, 8248–8278.

39 P. P. Shi, S. Q. Lu, X. J. Song, X. G. Chen, W. Q. Liao, P. F. Li, Y. Y. Tang and R. G. Xiong, *J. Am. Chem. Soc.*, 2019, **141**, 18334–18340.

40 X. J. Song, T. Zhang, Z. X. Gu, Z. X. Zhang, D. W. Fu, X. G. Chen, H. Y. Zhang and R. G. Xiong, *J. Am. Chem. Soc.*, 2021, **143**, 5091–5098.

41 M. K. Jana, R. Song, Y. Xie, R. Zhao, P. C. Sercel, V. Blum and D. B. Mitzi, *Nat. Commun.*, 2021, **12**, 4982.

42 Y. Yang, F. Lou and H. Xiang, *Nano Lett.*, 2021, **21**, 3170–3176.

43 X. Xiao, J. Zhou, K. Song, J. Zhao, Y. Zhou, P. N. Rudd, Y. Han, J. Li and J. Huang, *Nat. Commun.*, 2021, **12**, 1332.

44 Y. Fu, S. Jin and X. Y. Zhu, *Nat. Rev. Chem.*, 2021, **5**, 838–852.

45 D. W. Fu, H. L. Cai, Y. Liu, Q. Ye, W. Zhang, Y. Zhang, X. Y. Chen, G. Giovannetti, M. Capone, J. Li and R. G. Xiong, *Science*, 2013, **339**, 425–428.

46 Y. Zhang, Y. Liu, H. Y. Ye, D. W. Fu, W. Gao, H. Ma, Z. Liu, Y. Liu, W. Zhang, J. Li, G. L. Yuan and R. G. Xiong, *Angew. Chem., Int. Ed.*, 2014, **53**, 5064–5068.

47 P. A. Tanner, *Chem. Soc. Rev.*, 2013, **42**, 5090–5101.

48 Y. Zhang, W.-Q. Liao, D.-W. Fu, H.-Y. Ye, Z.-N. Chen and R.-G. Xiong, *J. Am. Chem. Soc.*, 2015, **137**, 4928–4931.

49 H.-Y. Ye, Q. Zhou, X. Niu, W.-Q. Liao, D.-W. Fu, Y. Zhang, Y.-M. You, J. Wang, Z.-N. Chen and R.-G. Xiong, *J. Am. Chem. Soc.*, 2015, **137**, 13148–13154.

50 Z. Wei, W. Q. Liao, Y. Y. Tang, P. F. Li, P. P. Shi, H. Cai and R. G. Xiong, *J. Am. Chem. Soc.*, 2018, **140**, 8110–8113.

51 Y. Zhang, W. Q. Liao, D. W. Fu, H. Y. Ye, C. M. Liu, Z. N. Chen and R. G. Xiong, *Adv. Mater.*, 2015, **27**, 3942–3946.

52 E. M. Sanchez-Carnerero, A. R. Agarrabeitia, F. Moreno, B. L. Maroto, G. Muller, M. J. Ortiz and S. de la Moya, *Chem. - Eur. J.*, 2015, **21**, 13488–13500.

53 G. Long, C. Jiang, R. Sabatini, Z. Yang, M. Wei, L. N. Quan, Q. Liang, A. Rasmita, M. Askerka and G. Walters, *Nat. Photonics*, 2018, **12**, 528–533.

54 J. L. Greenfield, J. Wade, J. R. Brandt, X. Shi, T. J. Penfold and M. J. Fuchter, *Chem. Sci.*, 2021, **12**, 8589–8602.

55 Y. Shi, P. Duan, S. Huo, Y. Li and M. Liu, *Adv. Mater.*, 2018, **30**, 1705011.

56 W. Chen, S. Zhang, M. Zhou, T. Zhao, X. Qin, X. Liu, M. Liu and P. Duan, *J. Phys. Chem. Lett.*, 2019, **10**, 3290–3295.

57 Y. H. Kim, Y. Zhai, E. A. Gaulding, S. N. Habisreutinger, T. Moot, B. A. Rosales, H. Lu, A. Hazarika, R. Brunecky, L. M. Wheeler, J. J. Berry, M. C. Beard and J. M. Luther, *ACS Nano*, 2020, **14**, 8816–8825.

58 G. Kresse and J. Furthmüller, *Comput. Mater. Sci.*, 1996, **6**, 15–50.

59 P. E. Blöchl, *Phys. Rev. B: Condens. Matter Mater. Phys.*, 1994, **50**, 17953–17979.

60 J. P. Perdew, K. Burke and M. Ernzerhof, *Phys. Rev. Lett.*, 1996, **77**, 3865–3868.

61 M. J. Frisch, G. W. Trucks, H. B. Schlegel, G. E. Scuseria, M. A. Robb, J. R. Cheeseman, G. Scalmani, V. Barone, G. A. Petersson, H. Nakatsuji, X. Li, M. Caricato, A. V. Marenich, J. Bloino, B. G. Janesko, R. Gomperts, B. Mennucci, H. P. Hratchian, J. V. Ortiz, A. F. Izmaylov, J. L. Sonnenberg, D. Williams-Young, F. Ding, F. Lipparini, F. Egidi, J. Goings, B. Peng, A. Petrone, T. Henderson, D. Ranasinghe, V. G. Zakrzewski, J. Gao, N. Rega, G. Zheng, W. Liang, M. Hada, M. Ehara, K. Toyota, R. Fukuda, J. Hasegawa, M. Ishida, T. Nakajima, Y. Honda, O. Kitao, H. Nakai, T. Vreven, K. Throssell, J. A. Montgomery, Jr., J. E. Peralta, F. Ogliaro, M. J. Bearpark, J. J. Heyd, E. N. Brothers, K. N. Kudin, V. N. Staroverov, T. A. Keith, R. Kobayashi, J. Normand, K. Raghavachari, A. P. Rendell, J. C. Burant, S. S. Iyengar, J. Tomasi, M. Cossi, J. M. Millam, M. Klene, C. Adamo, R. Cammi, J. W. Ochterski, R. L. Martin, K. Morokuma, O. Farkas, J. B. Foresman and D. J. Fox, *Gaussian 16, Revision B.01*, Gaussian Inc., Wallingford CT, 2016.

62 T. Lu and F. Chen, *J. Comput. Chem.*, 2012, **33**, 580–592.